SAND2016-2586J

Experimental Validation Data for Computational Fluid Dynamics of Mixed Convection on a Vertical Flat Plate

Blake W. Lance
Advanced Nuclear Concepts,
Sandia National Laboratories,
Albuquerque, NM 87185
e-mail: blance@sandia.gov

Jeff R. Harris
Applied Research Laboratory,
The Pennsylvania State University,
State College, PA 16802
e-mail: jeff.harris@psu.edu

Barton L. Smith
Professor
Fellow ASME
Mechanical and Aerospace Engineering,
Utah State University,
Logan, UT 84322
e-mail: barton.smith@usu.edu

Model validation for computational fluid dynamics (CFD), where experimental data and model outputs are compared, is a key tool for assessing model uncertainty. In this work, mixed convection was studied experimentally for the purpose of providing validation data for CFD models with a high level of completeness. Experiments were performed in a facility built specifically for validation with a vertical, flat, heated wall. Data were acquired for both buoyancy-aided and buoyancy-opposed turbulent flows. Measured boundary conditions (BCs) include as-built geometry, inflow mean and fluctuating velocity profiles, and inflow and wall temperatures. Additionally, room air temperature, pressure, and relative humidity were measured to provide fluid properties. Measured system responses inside the flow domain include mean and fluctuating velocity profiles, temperature profiles, wall heat flux, and wall shear stress. All of these data are described in detail and provided in tabulated format. [DOI: 10.1115/1.4032499]

1 Introduction

The purpose of this work is to provide validation data for three-dimensional CFDs models. Model validation will be discussed as well as the physical phenomenon of steady mixed convection. This work describes the experimental facility, the associated instrumentation, the BCs, the fluid and material properties, the test conditions, and the system response quantities (SRQs). This content follows the validation experiment completeness table of Oberkampf and Smith [1] to guide description of validation experiments. This guidance ensures that important details are included with a high level of completeness. The work contained herein is a continuation of that by Harris et al. [2] which covered forced convection using similar methods and facilities.

This work presents the data in table format for direct use in validating models. The provided data include the BCs and SRQs shown in Table 1. The BCs included in this work should provide modelers with all required information, remove the need for assumptions on model inputs, and reduce model form uncertainty [3]. The SRQ data are provided to modelers for direct comparison with model outputs. The experimental bias and random uncertainties of all data are also provided and quantified at the 95% confidence level. Validation errors can be calculated with the nominal data and validation uncertainty from the uncertainty of the nominal data [4].

These files are accessible in an online database in the Digital Commons of Utah State University's Library.[1] Links to specific files are included in this work with specific file names as to the data type (BC or SRQ), experimental case (buoyancy-aided or buoyancy-opposed), and measured quantity. Generally data are in table format as csv files. In addition to specific file links, all the files may be downloaded in the zipped file Files.zip.

1.1 CFDs Validation. To understand the need for experiments specifically aimed at providing validation data, one must first understand the different aims of validation and discovery experiments. Discovery experiments are common in research, where new physical phenomena are measured, presented, and discussed. Validation experiments do not necessarily measure unique phenomena, but the measurement process and description are more complete [5]. In general, older experimental data from discovery experiments are not sufficiently described for use in validation. Unobtrusive measurement techniques are important in validation experiments since probes introduce unknown uncertainties to the data. These uncertainties can only be mitigated by including the probe in the CFD model, which is usually unacceptably expensive.

The purpose of validation experiments is to provide the information required to quantify the uncertainty of a mathematical model. This uncertainty helps decision makers quantify model credibility. The ASME V&V 20 Standard [4] outlines an approach to estimate the validation comparison error and the validation uncertainty. The validation error E is the difference between the simulation result S and the validation experiment result D as

$$E = S - D \tag{1}$$

Calculating the validation uncertainty estimates the confidence interval of the error by considering both numerical and experimental uncertainty. Validation uncertainty is calculated as

$$U_{\mathrm{val}} = \sqrt{U_{\mathrm{num}}^2 + U_{\mathrm{input}}^2 + U_D^2} \tag{2}$$

where U_{num} is the numerical uncertainty, U_{input} is the model input uncertainty, and U_D is the experimental data uncertainty. The

Table 1 The tabulated BCs and SRQs provided in this work

BCs	SRQs
As-built geometry	Mean velocity profiles
Wall and inflow temps.	Fluctuating velocity profiles
Inflow mean velocity	Mean temperature profiles[a]
Inflow fluctuating velocity	Wall heat flux
Atmospheric conditions	Wall shear stress

[a]The SRQ time-mean air temperature profiles are provided for the buoyancy-opposed case only.

[1]digitalcommons.usu.edu/mae_facpub/2074/.

Manuscript received September 23, 2015; final manuscript received December 28, 2015; published online xx xx, xxxx. Assoc. Editor: Hugh W. Coleman.

numerical uncertainty is estimated from solution verification with sources such as iterative and discretization uncertainty. The latter two uncertainties come from the validation data. The uncertainty in the measured BCs that are used for model inputs is U_{input}. The uncertainty of SRQs—experimental data used to compare system outputs—is U_D. If $|E| \gg U_{\text{val}}$, one can conclude model error remains. But if $|E| \leq U_{\text{val}}$ and U_{val} is acceptably small for the intended use of the model, the validation error may be satisfactory. These general equations show validation data and their uncertainties are required to assess model accuracy via model validation.

There are several tiers of detail in validation experiments [6], often four as shown in Fig. 1. This work is considered a benchmark case that is second in simplicity to unit problems. The benchmark case, also called separate effects testing, requires that all model inputs and most model outputs are measured and that experimental uncertainty is included. In this tier, there is generally some level of multiphysics interaction, such as coupled fluid momentum and heat transfer, which prevents the study from being considered a unit problem. On the other hand, the nonprototypical geometry used in this work prevents consideration as a subsystem case.

In considering the design of validation experiments SRQs should be measured from a wide range and high difficulty in the difficulty spectrum as shown in Fig. 2. Comparing simulation results with the experimental data from a wide range on the spectrum increases the validation confidence. For example, integral quantities, such as fluid mass flow rate, generally have low experimental noise and random errors. Derivative quantities like fluid shear are more sensitive to nonideal conditions. If a model and data are in good agreement at a high level, then it is likely that good agreement will be observed in lower levels. But agreement at lower levels does not imply agreement at higher levels [3].

1.2 Mixed Convection. Mixed convection is a coupled fluid momentum and heat transfer phenomenon where both forced and natural convection contribute to behavior. With forced convection, buoyant forces are negligible and flow is driven by a pressure gradient. Conversely, buoyant forces drive natural convection in the direction opposite to gravity as low density fluid rises over higher density fluid [7].

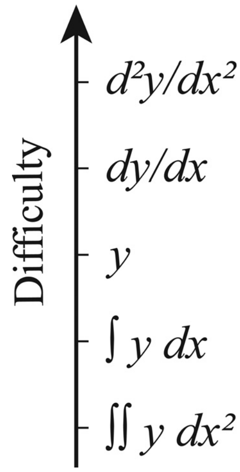

Fig. 2 SRQ difficulty spectrum, after Ref. [3]. The variables *y* and *x* here are arbitrary.

There are generally three types of mixed convection that depend on the relative direction of buoyant and pressure forces. The first is *buoyancy-aided*, where buoyant forces and forced flow have the same direction. The second is *buoyancy-opposed*, where these forces have opposite directions. Finally, the third is *transverse*, where these forces are perpendicular [8].

The mixed convection regime is defined by the local Richardson number as

$$\mathrm{Ri}_x = \mathrm{Gr}_x / \mathrm{Re}_x^2 \quad (3)$$

where

$$\mathrm{Re}_x = \overline{u}_{\text{bulk}} x / \nu \quad (4)$$

and

$$\mathrm{Gr}_x = g\beta (T_s - T_\infty) x^3 / \nu^2 \quad (5)$$

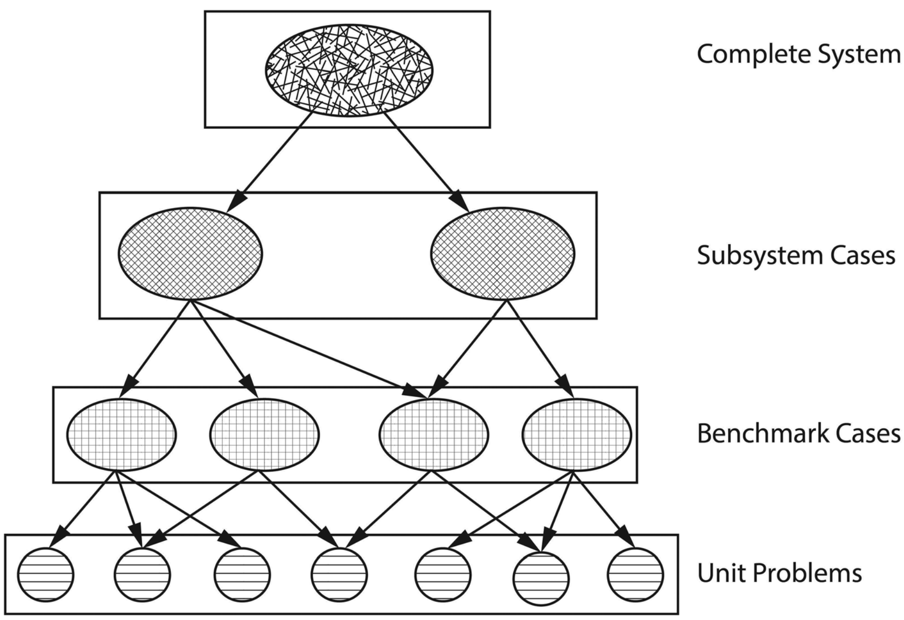

Fig. 1 The Validation Hierarchy, after Ref. [6]

In these equations, g is the acceleration due to gravity, β is the fluid thermal coefficient of expansion, T_s and T_∞ are the surface and fluid temperatures, respectively, x is the local streamwise location, ν is the fluid kinematic viscosity, and $\overline{u}_{\text{bulk}}$ is the bulk time-mean velocity. Mixed convection is commonly thought to occur for buoyancy-aided flow when $0.3 < \text{Ri}_x < 16$ and for buoyancy-opposed flow when $0.3 < \text{Ri}_x$ [7].

Some flow parameters in this study are given in Table 2. Note that external coordinates are used because the flow was not fully developed in the test section as it would be for pipe flow. The flow at x_1 was not in the mixed convection regime; but, as will be shown, buoyancy effects are still observable. The temperature of the heated wall was near the safety limit of the materials, and the air velocity was near the low side of the turbulent regime (large turbulent trips were installed upstream of the test section to enforce boundary layer turbulence at these lower Reynolds numbers).

There have been many mixed convection studies on vertical plates and in vertical tubes. Several mixed convection experiments for vertical tubes are cited in a review article by Jackson et al. [9]. They surveyed literature and presented results for both laminar and turbulent flows, both theoretical and experimental studies. Results were compared and heat transfer correlations presented. They noted that heat transfer in the buoyancy-aided turbulent flow is suppressed for moderate buoyancy levels while, on the other hand, it is augmented in buoyancy-opposed flows. This work provides heat transfer correlations for pipe flow that could be useful for comparison with the current work. They further recommend the use of Low Re models for mixed convection simulations.

Chen et al. [10] presented correlations for laminar mixed convection on vertical, inclined, and horizontal plates and compare them with the experiments performed by Ramachandran et al. [11]. Experiments of the latter provided point velocity and temperature measurements via a hot-wire anemometer. The data agreed very well with predictions and were sufficient for comparison to correlations but are not reported in sufficient detail for use as validation benchmarks.

Kim et al. [12] summarized simulations that predict mixed convection in a vertical tube and compared the models to experimental data. Their in-house code used published two-equation models and was written to model developing mixed convection flow with variable properties. Consistent with previous works, laminarization of the turbulent flow was reported in the buoyancy-aided case and increased turbulent levels in the opposed case. None of the investigated models showed good agreement over the entire range of flow, suggesting further model development, or perhaps model calibration, could increase prediction capability for these flows.

Wang et al. [13] discussed both an experimental and a numerical study of a vertical plate under turbulent mixed convection. Two-component laser Doppler anemometry was used to measure the boundary layer velocity. Some temperature measurements were also made of the flow using a thermocouple (TC) rake. They reported moderate agreement between experimental data and simulation results, but noted that predictions for the buoyancy-opposed case were less accurate. Although this study provides valuable insight into this flow with plate geometry, the reported information lacks BCs and inflow parameters necessary for validation benchmarks.

Table 2 Re_x, Gr_x, and Ri_x at the three locations in x at the spanwise center where SRQ data were acquired. The bulk velocity $\overline{u}_{\text{bulk}}$ was 2.44 m/s. These apply for both cases presented.

	x (m)	Re_x	Gr_x	Ri_x
x_1	0.16	13,000	1.55×10^7	0.09
x_2	0.78	63,000	1.73×10^9	0.43
x_3	1.39	110,000	9.93×10^9	0.77

Mixed convection literature is abundant. However, all the papers found were performed as discovery experiments rather than for the purpose of providing validation data. Most are for pipe flow, boundary and initial conditions are lacking, uncertainties are rarely presented, flow geometry description is simplified, and fluid properties are seldom given. Further, the techniques used were often intrusive, leading to the unknown uncertainties. Modern measurement systems can provide higher fidelity data while disrupting the flow less.

2 Experimental Facility

All experiments were performed in the Rotatable Buoyancy Tunnel (RoBuT), which will be described in detail. Benchmark-level validation data were acquired with simple geometry and some multiphysics interaction. The square test section allowed easy characterization using optical velocity measurements. The simple geometry is easy to represent numerically and helps isolate model errors.

2.1 Rotatable Buoyancy Tunnel. The RoBuT was an open-circuit air tunnel with a large 4.81 m diameter "Ferris wheel" design that allowed rotation, thus changing the relative direction of forced flow and buoyant forces without changing the facility. Many important tunnel components are shown in Fig. 3, which is in the buoyancy-aided orientation. Note the coordinate system

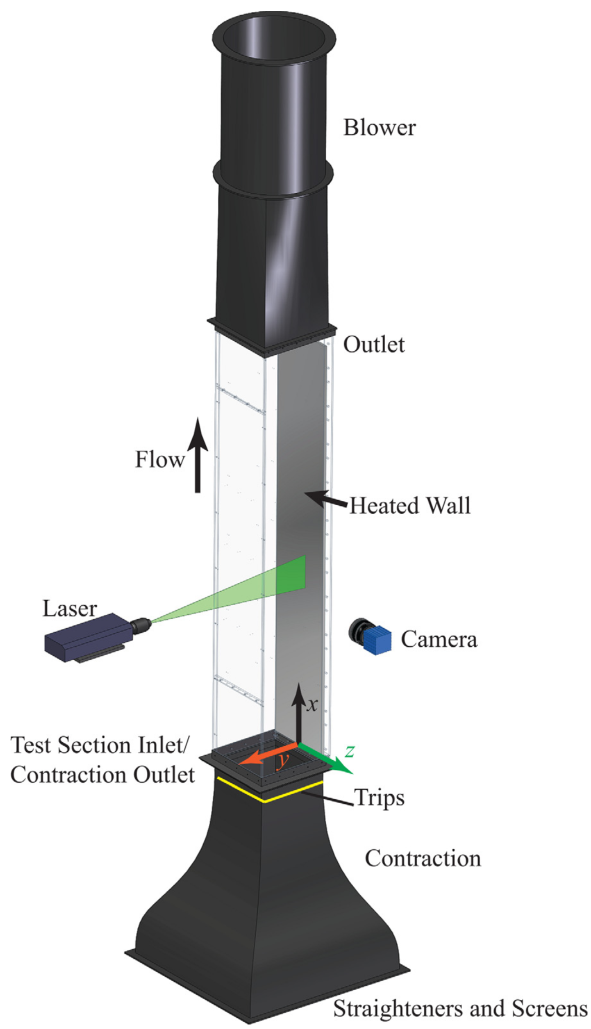

Fig. 3 RoBuT flow components in the buoyancy-aided orientation

with the origin on the heated wall at the inlet and the spanwise center. The streamwise distance is x, wall-normal distance is y, and spanwise distance is z with zero along the centerline. The laser and camera were part of a particle image velocimetry (PIV) system that will be described in Sec. 3.2.

The test section had a 0.305×0.305 m square cross section and was 2 m long. It had three clear walls for optical access and a heated wall for a thermal BC. More details of the test section are provided in Sec. 2.2. The contraction and outlet were made of fiberglass-reinforced plastic with a glass-smooth, black gel-coat.

The contraction had an area ratio of 6.25:1 and was 0.914 m long. The contraction bell at the leading edge had a 102 mm radius. Between the contraction and bell were four modular sections that contained—in order of flow direction—a single row, aluminum fin/copper tube, chilled water heat exchanger (Super Radiator Coils Model 30x30-01 R-0.625/048); a settling length section; a precision aluminum honeycomb flow straightener; and two high porosity screens. Square turbulence trips 3.175 mm wide were installed along all four walls and located 0.12 m upstream of the test section inlet.

The outlet expanded the flow downstream of the test section, had a total included angle of 8.2 deg, and was 0.686 m long. The blower drew air through the test section and rejected it into the room. It included an inline centrifugal fan assembly, TCF/Aerovent model 14-CBD-3767-5. It was belt driven by a 5 HP, TEFC, 230-460 VAC induction motor, Toshiba model B0052FLF2AMH03. The motor was powered by a Toshiba variable frequency drive, model VFS11-2037PM-WN.

Two Laskin Nozzles [14] were used to atomize olive oil tracer particles. These were measured to have a mean diameter of about 1 μm with a TSI aerodynamic particle size spectrometer at the outlet. These particles were mixed with air and injected into a PVC pipe distribution system upstream of the contraction assembly. A peg board was placed between this system and the beginning of the contraction to help mix particles throughout the flow. It had holes 6.35 mm in diameter that were spaced 25.4 mm apart in a square pattern.

2.2 Test Section. The test section had four walls, an inlet, and an outlet. The heated wall was custom designed to provide a heated surface for convection and featured embedded instrumentation. Its cross section is shown in Fig. 4. This wall was heated to approximately 138 °C for this study. It was made of several layers of aluminum, had six silicon rubber heaters arranged in the streamwise direction, and contained thermal insulation to drive most of the heat inward. A list of materials and thicknesses is available in Table 3. The surface was nickel plated to reduce thermal radiation which resulted in a predicted and measured emissivity around 0.03 [2]. Aluminum 2024, though more expensive than the common alloy 6061, was used because its thermal conductivity is better known [15]. The heated portion was 279 mm wide and 1.89 m long. The left and right spanwise sides were thermally insulated by 17.5-mm thick Teflon® that extended into grooves in the side walls. Two additional 12.7-mm thick Teflon® insulators were placed upstream and downstream of the heated wall. There were six heaters, each spanning the width of the heated wall and one sixth of the length. Three HP 6439B power supplies were connected to two heaters each and were used to control the temperature of the wall via a closed-loop proportional-integral-derivative (PID) controller. Three controllers, one for each power supply, allowed the heated wall to be heated in independent sections in the streamwise direction to increase temperature uniformity.

The other three walls were clear Lexan® polycarbonate for optical access and were 12.7 mm thick. From the perspective of standing on the heated wall at the inlet, they are termed left ($z = -152$ mm), top ($y = 305$ mm), and right ($z = 152$ mm) walls. The top wall had a removable center portion for cleaning and

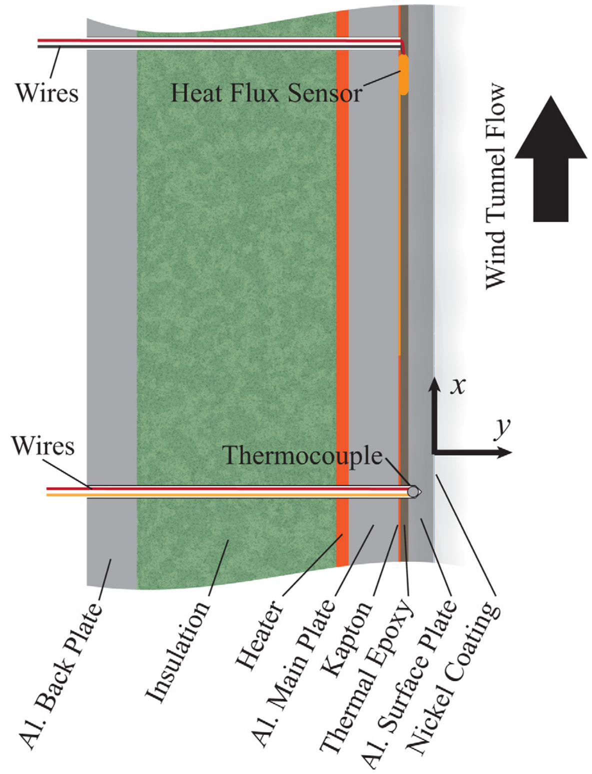

Fig. 4 Heated wall cross section with component names as in Table 3. The relative thicknesses are to scale.

Table 3 Heated wall components and thicknesses with names from Fig. 4

Name	Material	t (mm)
Nickel coating	Bright nickel	~0.05
Al. surface plate	Al. 2024-T3	3.18
Thermal epoxy	Dow corning 3-6751	1.02
Kapton®	Kapton® HN film	0.254
Al. main plate	Al. 6061-T651	6.35
Heater	Tempco silicone rubber	1.59
Insulation	Mineral wool	25.4
Al. back plate	Al. 6061-T651	6.35

maintenance. This wall also had three 25.4-mm ports for probe insertion that were used for the TC probe described in Sec. 3.3.

The as-built geometry was measured to compensate for the differences between the as-designed and as-built test section geometry. The differences were small, but the measurements are presented for completeness. An internal micrometer was used to measure the internal dimensions of the fully assembled test section. Height measurements were performed at the left, center, and right as well as width measurements at the top, middle, and bottom. This was done at seven locations in x and performed three times for an estimate of random uncertainty. Modelers may use these dimensions when constructing the simulation domain to ensure greater similarity. A sketch of the measurement locations may be accessed from the online database by the link BC-As-built Sketch in the digital version of this work. The nominal values are in BC-As-built Measurements and uncertainties in BC-As-built Measurement Uncertainties.

A warm-up procedure was followed each time the RoBuT was used for experiments. The heated wall was first heated to the set-point temperature. Once this was reached, the blower was set to the desired speed for the experiment and the heater controllers would accordingly increase power. Once the temperature was again stable for at least 5 min, the facility was ready for data acquisition. If the blower setpoint speed was changed, the controller would stabilize temperature and a waiting period was repeated for at least 5 min.

Between data acquisition for the different cases, such as between the buoyancy-aided and opposed cases, the entire test section was cleaned with Ethyl Alcohol to ensure optical quality. The cover on the top wall was removed for cleaning inside. High-vacuum grease was used on test section joints to eliminate air leakage and was removed and reapplied each time a panel of the test section was adjusted.

3 Analog Instrumentation and Signal Processing

Validation experiments require high fidelity instrumentation. TCs were used to measure boundary temperatures, heat flux sensors (HFSs) for heat flux through the heated wall, and PIV for inflow and boundary layer air velocity. Other sensors measured room air conditions. These systems will now be described in detail.

3.1 Thermal Instrumentation. A total of 307 TCs were used to measure boundary temperatures. All test section TCs were 30 gauge Type K from Omega Engineering with Special Limits of Error. They were each welded to length with an Argon-shielded welder. Each TC was calibrated with an Isotherm FASTCAL-M with an accuracy of 0.3 °C over a range of 25–190 °C with data at every 5 °C. Because every TC calibration was very similar and made from the same spool, an average calibration curve was applied. An array of 3×5 TCs, three in y and five in z, was suspended on the downstream side of the honeycomb for inlet air temperature measurements. Each of the three clear walls had 21 TCs with seven rows spaced in x and three across in y for the left and right walls or in z for the top wall. The bulk of the heated wall had 5×32 TCs with five in z and 32 in x. The Teflon® edges each had embedded TCs with five across the leading edge in z and 32 along the sides in x. All TCs were embedded to within 3.18 mm of the inside surface using thermal epoxy with enhanced thermal conductivity.

Three HFSs were embedded into the heated wall along the spanwise center at the x-locations found in Table 2. They were model 20457-3 from RdF Corporation and were a thin-film type with a thermopile around a Kapton® substrate. The manufacturer supplied unique calibration coefficients for each sensor. The manufacturer-specified uncertainty was 5% of reading. An embedded Type T TC was used to measure sensor temperature and correct readings with the supplied multiplication factor curve to compensate for changes in thermal conductivity of the substrate. The HFSs were placed adjacent to the Kapton® layer of similar thermal resistance to reduce measurement errors. A thermal resistance network analysis showed only a 2.4% difference in heat flux between HFS and non-HFS conduction paths.

The TC and HFS output voltages were small, so special data acquisition (DAQ) devices were selected. National Instruments (NI) products were used as they interfaced well with the LABVIEW software that was employed for system control and thermal data recording. Twenty-one NI-9213 TC modules were housed in five NI-cDAQ-9188 chassis. The narrow voltage range of ±78 mV, 24-bit analogue to digital conversion and open channel detection made them well suited for these measurements. A built-in cold junction compensation (CJC) was used for TCs. The total uncertainty of the calibrated TCs with these DAQs was 1 °C, largely attributable to the CJC uncertainty of 0.8 °C. Data from thermal instrumentation was recorded on-demand. Twelve sets of instantaneous measurements were recorded, one to accompany every set of PIV data for each case.

3.2 PIV. The PIV system allowed for nonintrusive, full-field velocity measurements at several locations. The system consisted of a laser, camera, and timing unit. The laser was a New Wave Research Solo PIV III. It was a dual cavity, frequency-doubled Nd:YAG model with about 22 mJ/pulse and a wavelength of 532 nm. Two LaVision camera designs were used as the equipment was upgraded: an Imager Intense charge-coupled device (CCD) camera for buoyancy-aided data and an Imager sCMOS for buoyancy-opposed data. The former had a 12-bit CCD sensor with 1376×1040 pixels and a pixel size of 6.45 μm. The latter had a 16-bit sCMOS sensor with 2560×2160 pixels and a pixel size of 6.5 μm. An internal, LaVision standard version PTU 9 timing unit provided accurate timing of the system and had a resolution of 10 ns and jitter of <1 ns. Two Nikon lenses were used: one AF Nikkor 28 mm f/2.8 D for the large field of view inflow and one AF Micro-Nikkor 105 mm f/2.8 D for high resolution SRQ data near the heated wall.

Images were acquired with LAVISION DAVIS 8.1 software and processed with DAVIS 8.2. The optical configuration of the system is shown in Fig. 3 with the laser sheet normal to the heated wall and camera viewing angle parallel with it. The equipment was moved manually in the x direction. The inflow was measured in the same configuration with Velmex BiSLide® traverses to move the laser and camera consistently in the z direction. In this way, nine planes were measured to map the inflow.

PIV calibration was performed in two ways. The inflow measurement used a conventional two-component "ruler" calibration over a span of about 280 mm since the laser sheet and camera were normal to each other. The SRQ data near the heated wall was calibrated with a single-plane calibration target and the pinhole model as the camera was angled into the wall by 3–5 deg. This angle was required to avoid image diffraction by the large temperature gradient very near the wall. Because this flow had very little through-plane motion, errors in v velocity from through-plane motion appearing as in-plane motion are expected to be small (they are a function of the sine of the angle). The pinhole model was applicable since refraction between the Lexan® and air was also small.

Prior to acquisition, the quality of the particle images was checked to ensure proper particle density, diameter, and displacement as well as laser beam overlap and image focus quality. Many of these data parameters and others from the acquired images are found in Table 4. The diameter, density, and displacement are spatial averages over the entire image. Both particle diameter and

Table 4 PIV data parameters. Aided refers to buoyancy-aided case while opposed refers to buoyancy-opposed case.

Parameter	Aided-inlet	Opposed-inlet
N image pairs	500	1000
Sample frequency (Hz)	4	10
dt (μs)	1000	750
Lens	28 mm	28 mm
Extension (mm)	—	—
Calibration (mm/pixel)	0.223	0.124
f#	5.6	11
Diameter (pixels)	1.45	1.39
Density (#/32×32)	70.8	19.3
Displacement (pixels)	11.4	15.7
Parameter	**Aided-SRQ**	**Opposed-SRQ**
N image pairs	1000	1000
Sample frequency (Hz)	4	10
dt (μs)	76	62–65
Lens	105 mm	105 mm
Extension (mm)	39.5	39.5
Calibration (mm/pixel)	0.0116	0.0103
f#	5.6	11
Diameter (pixels)	3.98–4.89	3.07–3.16
Density (#/32×32)	6.36–8.99	4.76–8.47
Displacement (pixels)	13.8	12.2

density were determined by the methods found in Ref. [16] with the local maximum method for density estimation.

The processing of particle images was performed with the window deformation method in DAVIS. A mask was carefully defined to remove the influence of walls on the correlation. Round interrogation windows were used for reduced noise. The first two passes were at 64×64 pixels and 75% overlap and the final four passes were at 32×32 pixels and 75% overlap. Vector postprocessing was performed, where vectors were removed if the peak ratio was less than two. Then a two-pass median filter of "strongly remove and iteratively replace" corrected spurious vectors. Vectors were removed if their difference from average was more than one standard deviation of neighbors and subsequently replaced if the difference from average was less than two standard deviations of neighbors.

Particle images had a sliding background removed where the background is the average of nine images symmetrically taken around the image of interest. The pixel range was sometimes narrowed in the flow direction to reduce disk space while keeping at least 512 pixels in this direction. Examples of particle images with background subtracted for both orientations acquired with two cameras are shown in Fig. 5. Note that the heated wall is on opposite sides since the tunnel orientation was changed between cases. Also, the buoyancy-aided case used the Imager Intense camera with fewer pixels than the sCMOS used in the buoyancy-opposed case.

3.3 TC Probe. In order to provide an additional SRQ, the fluid temperature in the boundary layer was measured. Since the RoBuT is an open-loop air tunnel with a large volume flow rate, optical measurement techniques requiring specialized particles are not practical. Thus, a TC probe was designed similar to that used in Ref. [17] with the care taken to reduce the size and subsequent disruption of the flow. As this probe was intrusive and changed the flow, it was used after acquiring all other types of data so that its influence is only seen on the temperature profiles.

The junction of the probe was formed by type K wires of diameter $D_{TC} = 0.051$ mm from Omega Engineering. The two lead wires are aligned parallel to the wall with a length of 15.3 mm ($\sim$300 D_{TC}) to reduce conduction losses as shown in Fig. 6. The junction was formed by spot welding the overlapped wires. After welding, the wire was pulled taut and epoxied in place. The fine wire was welded to thicker 0.511-mm wire that spanned the pivot and was connected to the DAQ. The brace shown in Fig. 6 was rigid enough to keep the wire tight. To correct the small misalignments that could cause measurement errors, a pivot was designed into the probe so it could be aligned with the wall before each measurement. This was done by moving the probe into the wall until both ends of the brace were pressed firmly and any error corrected, then pulling the probe away from the wall. This probe voltage was measured with the same NI-9213 TC modules described in Sec. 3.1 and was used in the spanwise center of the tunnel.

The probe may be subject to conduction losses that could lead to measurement error. This error was estimated using a 1D fin equation. The measured temperature and velocity profiles were used to estimate fluid properties and heat transfer coefficients. Heat conduction was considered from the TC junction to the leads and then convecting to the lower temperature air. The largest error was estimated at 0.03 °C at the wall at x_1.

This TC probe assembly was supported by a stainless steel tube with 3.76 mm outside diameter that spanned the test section. This tube contained the TC wires and was connected to a Velmex Inc. UniSlide® traverse model B4015Q2J. This traverse was used for small, incremental movements. The distance from the wall was estimated by fitting a line to the temperature profile very near the wall to the wall temperature measured by embedded TCs. The largest uncertainty in position resulted from the stepper motor resolution. With 200 steps/rev. and an assumed 1/2 step resolution, the uncertainty was 2.5 μm. The pitch uncertainty was much smaller at 0.04 mm/25.4 cm or 0.0315 μm for a 200 μm step.

3.4 Atmospheric Instrumentation. Air temperature, relative humidity, and atmospheric pressure in the RoBuT room were measured to determine air properties. Both temperature and humidity were measured with an Omega HX93A probe. Pressure was measured with an Apogee Instruments BPS 1006 sensor. The output voltage of these sensors was measured by an NI USB-9215 A 4-channel $\pm$10 V analog input DAQ. The uncertainty of temperature was 0.6 °C, humidity was 2.5% for readings 20–80% and 3.1% otherwise, and pressure was 3% of reading. These data were sampled at 1 Hz, then averaged and recorded once per minute.

3.5 Uncertainty Quantification (UQ). Thermal and atmospheric data UQ was determined following the methods of Coleman and Steele [18]. UQ for PIV was considered by other

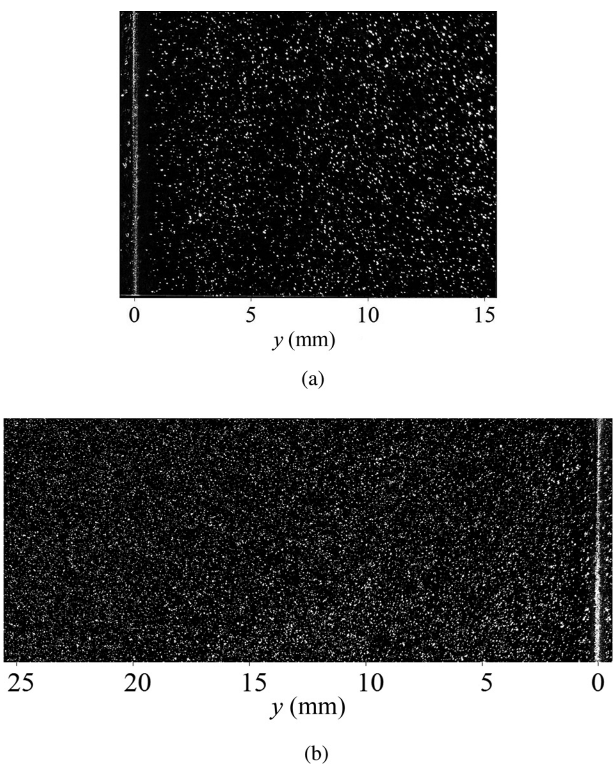

Fig. 5 Particle images at x_2: (*a*) buoyancy-aided with heated wall at left and (*b*) buoyancy-opposed with heated wall at right

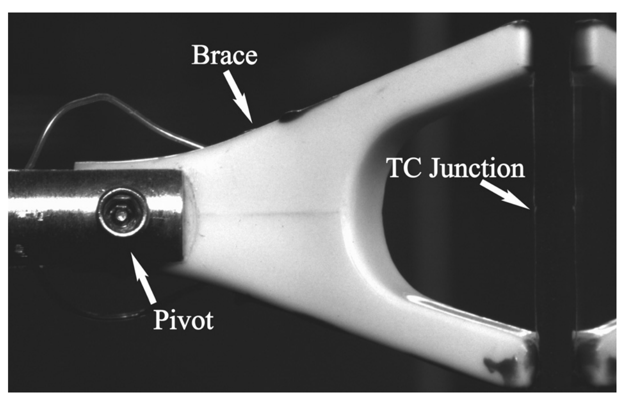

Fig. 6 TC probe with its reflection in the heated wall on the right

methods and is described later. Bias uncertainties were obtained from sensor documentation at the 95% confidence level. The standard random uncertainty of a general mean quantity $\overline{x}$ was calculated by

$$s_{\overline{x}} = \frac{s_x}{\sqrt{N}} \qquad (6)$$

where s_x is the sample standard deviation. Standard bias and random sources are combined to give the expanded total uncertainty as

$$U_{\overline{x}} = t_{95}\sqrt{b_{\overline{x}}^2 + s_{\overline{x}}^2} \qquad (7)$$

where t_{95} is the confidence level coefficient (taken as 1.96 for 95% confidence and number of samples $N > 30$) and $b_{\overline{x}}$ is the standard bias uncertainty of the mean. The data provided with this paper generally specifies the expanded (95% confidence) bias ($B_{\overline{x}}$), random ($S_{\overline{x}}$), and total uncertainty ($U_{\overline{x}}$) values with the mean results.

Uncertainty of the PIV results was calculated from the Uncertainty Surface Method that estimates instantaneous bias and random uncertainties due to the effects of particle displacement, particle image density, particle image size, and shear. This method was originally described in Ref. [19] and improved with the methods from Ref. [16]. The uncertainties of the velocity statistics propagated from the instantaneous uncertainties were calculated by the methods of Wilson and Smith [20]. Total uncertainty was calculated as in Eq. (7). The confidence level on all the UQ results in this work is 95%.

4 BCs

This section contains a description of all expected requisite BCs for CFD model inputs. The types of BCs were shown in Table 1. The as-built geometry is a BC, but was discussed previously in Sec. 2.2.

4.1 BC Description. The measured BC temperatures are mapped onto the test section geometry in Fig. 7. Note the higher measurement resolution on the heated wall compared to the other walls and the development of the thermal boundary layer on the right wall as air travels from the inlet to the right of the figure.

As mentioned previously, the inflow was measured in nine planes spaced in z with the planes concentrated near the side walls. The time-mean streamwise velocity $\overline{u}$ at the inlet is shown in Fig. 8 for the buoyancy-opposed case. Gray lines indicate PIV measurement locations that span across y. Data are highly resolved in y but not in z. Data may be interpolated from the information given. Another approach is to use the high-resolution data near the unheated top wall ($y = 305$ mm) boundary layer to the left and right walls which are also unheated. The flow at the inlet has been confirmed in Ref. [2] to be symmetric at the inlet.

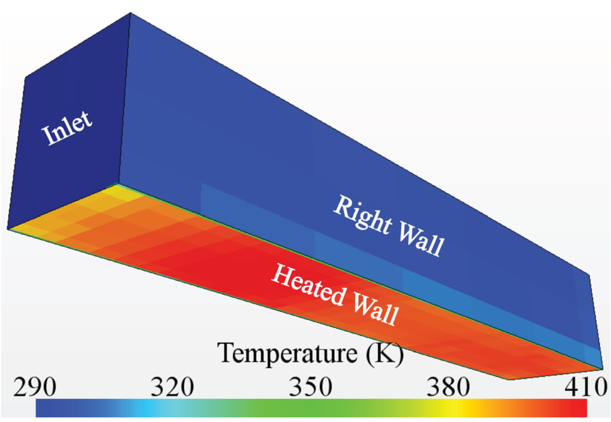

Fig. 7 Measured temperatures on the test section boundaries

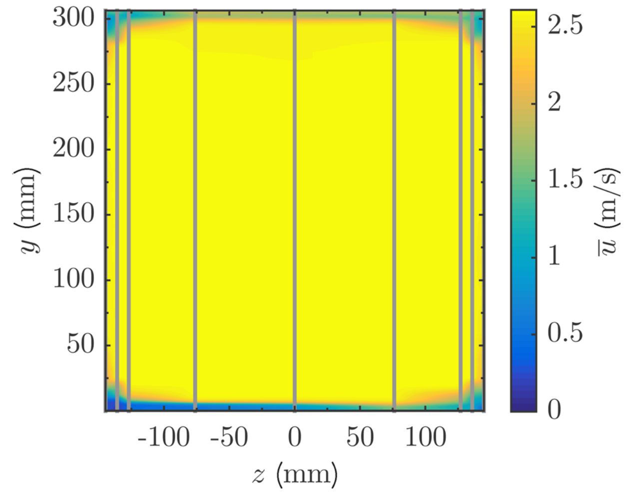

Fig. 8 Measured streamwise velocity $\overline{u}$ at the inlet for the buoyancy-opposed case

The atmospheric conditions include atmospheric pressure, relative humidity, and room temperature and were recorded at the time of data acquisition.

Test procedures were followed to control test conditions. The following list describes the steps followed for acquisition of both BC and SRQ data:

(1) Begin heating of the heated wall.
(2) Upon reaching setpoint temperature, start blower.
(3) Align traverses, laser, and camera with test section at measurement location.
(4) Align laser sheets.
(5) Focus camera on particle images.
(6) Align calibration plane with laser sheet and calibrate camera.
(7) Determine optimal dt for particle displacement, proper seeding density, and proper laser intensity.
(8) Record measurement location and other PIV parameters.
(9) Confirm stability of wall temperature and room conditions.
(10) Record PIV data, atmospheric and thermal conditions.

This process was repeated for PIV measurement locations for the nine inflow and the three SRQ data sets. Inflow data were acquired in a single day, so only the last three steps were repeated after the first set. PIV data were recorded at twelve locations (nine at the inlet and three along the heated wall). Atmospheric conditions and thermal measurements were recorded with each PIV data set.

Since the velocity at the inlet is partially developed, some external flow parameters are included. The momentum thickness was measured from PIV data at the spanwise center ($z = 0$) location using the integral

$$\delta_2 = \int_0^\infty \frac{\overline{u}}{\overline{u}_\infty}\left(1 - \frac{\overline{u}}{\overline{u}_\infty}\right) dy \qquad (8)$$

where $\overline{u}_\infty$ is the freestream velocity and constant density has been assumed [7]. The boundary layers on both walls were considered from $y = 0$–0.305 m and the result divided by two. Constant density is a good approximation at the inlet but not for downstream locations where the near-wall air was heated.

The concept of a virtual origin may also help predict the equivalent length of a flat plate extending upstream of the test section inlet. This allows for the impact of the contraction to be assessed. Assuming the flow was always turbulent, others have derived the relationship [7]

$$\frac{\delta_2}{x} = \frac{0.036\nu^{0.2}}{\overline{u}_\infty^{0.2} x^{0.2}} = 0.036\mathrm{Re}_x^{-0.2} \qquad (9)$$

The left two portions can be arranged to isolate x as in

$$\xi = \frac{\delta_2^{1.25} \overline{u}_\infty^{0.25}}{0.0157 \nu^{0.25}} \tag{10}$$

where ξ has been substituted for x and is the distance upstream to a virtual origin given δ_2 defined earlier. The results from these analyses are given in Table 5. It is reasonable to add these virtual origin distances to the x values in Table 2 when comparing with the more canonical flows. Also, Re_x and subsequently Ri_x numbers may also be adjusted. It is reasonable that the buoyancy-opposed case had a larger boundary layer at the inlet in this low speed flow as this case showed larger boundary layers downstream.

4.2 BC Data. These data are available for both the buoyancy-aided and opposed cases on the inflow and all four walls of the test section. There is one file for the measured temperature of each surface that can be found in Table 6. The files may be opened by the links in the digital version. The format for all BC files works directly with Star-CCM+ and is easily adaptable to other CFD codes. The columns X, Y, and Z are used throughout this work based upon the global coordinates and are presented in meters. The column "T[K]" is the mean temperature in Kelvin, "B_T[K]" is the bias uncertainty, "S_T[K]" is the random uncertainty, and "U_T[K]" is the total uncertainty.

The data for the inflow mean and fluctuating velocities are found in the files BC-Aid-Inlet-Vel and BC-Opp-Inlet-Vel. The columns "u," "v," and "w" are time-mean velocities in the x, y, and z directions, respectively. The columns "u′u′," "v′v′," "w′w′," and "u′v′" are specific Reynolds stresses. Uncertainties of $\overline{u}$, $\overline{v}$, and $\overline{w}$ compose the remaining columns. Reynolds stresses have unique upper and lower uncertainties with "Uuup" being the plus uncertainty of $\overline{u'u'}$ and so on. The units of velocity and velocity uncertainty are (m/s) while those of Reynolds stresses and their uncertainty are (m^2/s^2).

Note that inflow out-of-plane velocities $\overline{w}$ and $\overline{w'w'}$ were assumed to be the same as $\overline{v}$ and $\overline{v'v'}$, respectively. This assumption was proved valid in previous forced convection work in this facility by measuring the inflow in both directions with two-component PIV and comparing data where the measurement planes intersect [2]. As the inflow has little dependence on downstream conditions, this is still valid for mixed convection. Buoyancy-aided inflow data for the plane nearest the right wall was questionable and replaced with data nearest the left wall. As the geometry and thermal conditions are symmetric about $z = 0$, this was justified.

The atmospheric measurements, together with their uncertainties, are found in the files BC-Aid-AtmCond and BC-Opp-AtmCond.

Table 5 Boundary layer analysis results

Parameter	Aided	Opposed
δ_2 (mm)	1.61	1.81
ξ (mm)	417	485

Table 6 Links to temperature boundary files for both cases

Aided	Opposed
BC-Aid-InletTemp	BC-Opp-InletTemp
BC-Aid-HeatedWallTemp	BC-Opp-HeatedWallTemp
BC-Aid-LeftWallTemp	BC-Opp-LeftWallTemp
BC-Aid-TopWallTemp	BC-Opp-TopWallTemp
BC-Aid-RightWallTemp	BC-Opp-RightWallTemp

5 Fluid and Material Properties

As air is the working fluid, measurements of temperature, pressure, and relative humidity discussed in Sec. 4.2 are satisfactory to define all fluid properties. It is important to note that the working pressure is different from that at sea level as the experiment was conducted in Logan, Utah, which is 1460 m above sea level.

Material properties of the test section can easily be obtained from the information provided in Sec. 2.2 about the construction of the test section. It is not necessary to model the heated wall since temperature measurements were made very near the surface, but the information is provided for completeness.

6 Test Conditions

The RoBuT room was configured with modern heating and air conditioning systems and thermal insulation for stable conditions. Controls were independent of other systems in the building. The refrigerated air conditioning had a ~0.56 °C (1 °F) deadband. To reduce the rate of temperature change from the on/off behavior of this system, outside air was mixed with refrigerated air before being injected into the room. Heating was performed with a steam heat exchanger with attached fan. The original fan and control system were replaced with a variable speed, tuned, PID-controlled system implemented with the main LABVIEW program, giving the heating system tight control of the room temperature. The maximum measured temperature spread for both cases near the inflow location during DAQ is 0.7 °C (~1.3 F).

7 SRQs

The SRQs are the experimental results used to compare with simulation outputs and were listed in Table 1. Since they are similar, the mean velocity profiles and fluctuating velocity profiles in the form of Reynolds stresses are presented together. Temperature profiles from the TC probe are presented for the buoyancy-opposed case. Additionally, scalars of wall heat flux and wall shear stress are also provided.

7.1 SRQ Description. Normalized streamwise velocity and Reynolds stress for the buoyancy-aided and buoyancy-opposed cases are shown in Figs. 9 and 10, respectively, for three measurement locations in x. The bulk velocity $\overline{u}_{\mathrm{bulk}} = 2.44$ m/s was measured across the inlet and is used for normalization. The profile locations correspond to the vertical center of the camera sensor for reduced perspective error. Uncertainty bands are provided on both profiles that are unique for each data point. In other words,

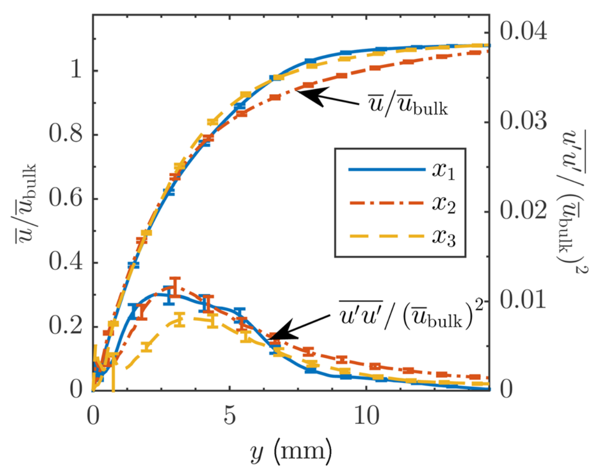

Fig. 9 Normalized streamwise mean velocity $\overline{u}$ and Reynolds normal stress $\overline{u'u'}$ at three locations in x for the buoyancy-aided case

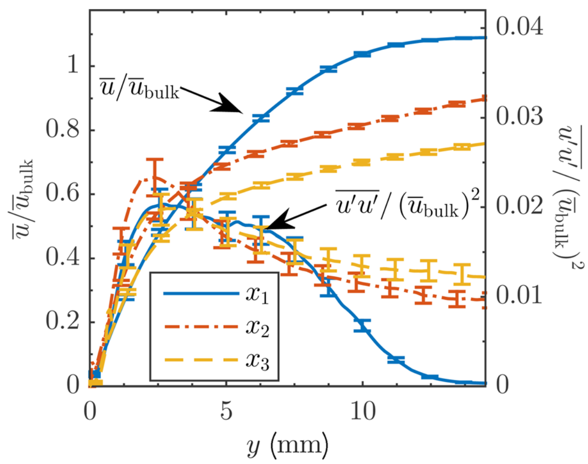

Fig. 10 Normalized streamwise mean velocity $\overline{u}$ and Reynolds normal stress $\overline{u'u'}$ at three locations in x for the buoyancy-opposed case

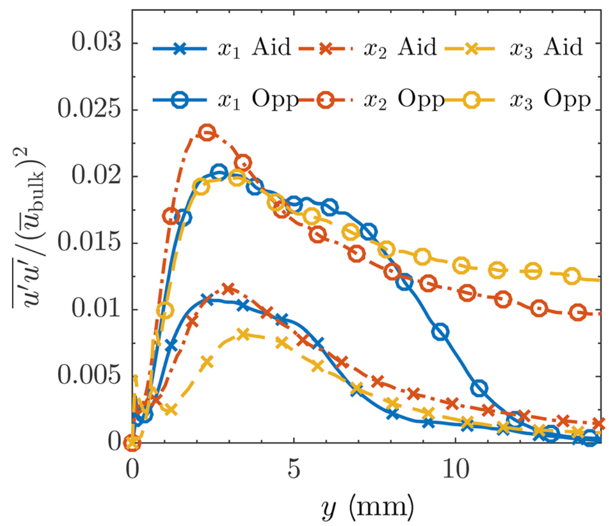

Fig. 12 Measured streamwise Reynolds normal stress $\overline{u'u'}$ with buoyancy-aided (Aid) and buoyancy-opposed (Opp) at three locations in x

the uncertainty of $\overline{u}/\overline{u}_{\mathrm{bulk}}$ and $\overline{u'u'}/(\overline{u}_{\mathrm{bulk}})^2$ varies over y. Uncertainty bands are subsampled for clarity.

The influence of buoyancy is apparent in several regards. The boundary layer velocity and Reynolds stress are nearly constant for all x in the buoyancy-aided case, indicating little growth in the boundary layer thickness. The buoyancy-opposed case, however, shows rapid boundary layer growth. Also apparent is evidence of laminarization in the buoyancy-aided case relative to that in the opposed case as seen in the Reynolds stresses. This is typical of mixed convection flows as described in previous works [9,12]. There are small differences in turbulence levels in the streamwise direction for each case that suggest boundary layer development and buoyancy influence change along the plate. One measure of this is wall shear that will be quantified in the data of Sec. 7.2.

The difference in the two cases reveals the influence of buoyancy on streamwise velocity and streamwise Reynolds normal stress. This is shown in Figs. 11 and 12, respectively. Buoyancy effects accelerate the boundary layer velocity, but this influence is localized near the heated wall. As in the findings of other researchers in mixed convection, turbulence levels as quantified by $\overline{u'u'}$ are increased for the opposed case. Here, the difference is about a factor of 2. There is a subtle two-peak nature to $\overline{u'u'}$ that is most apparent at x_1. This may be caused by the 3.175-mm-wide turbulence trips that are upstream of the test section, especially considering that this profile feature dies out farther downstream.

The measured temperature profile from the TC probe for the buoyancy-opposed case is shown in Fig. 13. The development of the thermal boundary layer is observable in x. The temperature in the near-wall region and line fit are shown in Fig. 14. Errors in distance from the wall are corrected by fitting the line through the measured wall temperature. The first point is not considered as it is likely to have position error. Only data within $y^+ \leq 6.6$ are used in the fit as they should be within the inner portion of the viscous or laminar sublayer where linear temperatures are expected. Temperature fluctuations are not included as the mass of the TC wire rendered it insensitive to the higher frequencies in this flow. These frequencies were determined with a 50.8 μm diameter tungsten hot-film probe with much less thermal mass.

The intrusive nature of the probe caused an increase in wall heat flux observable in the HFS data acquired at the time. The largest error of wall heat flux occurred when the probe was touching the heated wall and steadily decreased as the probe was retracted from the wall. Maximum errors of 18.7%, 10.4%, and 7.93% were measured at locations x_1, x_2, and x_3, respectively. This effect will only bias the temperature data provided as all other BC and SRQ data were acquired at other times. Intrusive

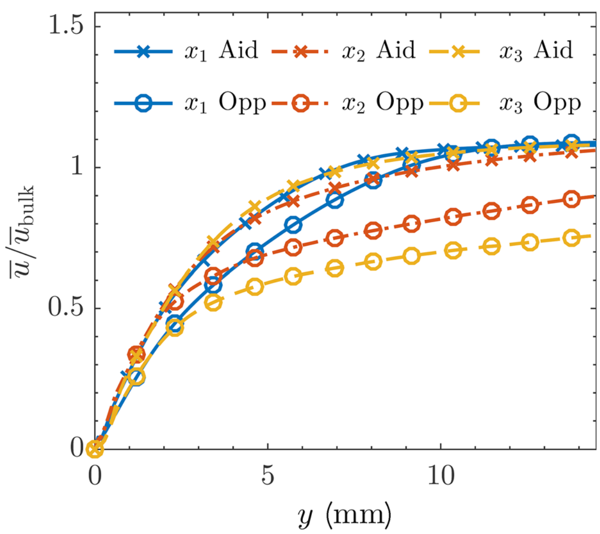

Fig. 11 Measured streamwise mean velocity $\overline{u}$ with buoyancy-aided (Aid) and buoyancy-opposed (Opp) at three locations in x

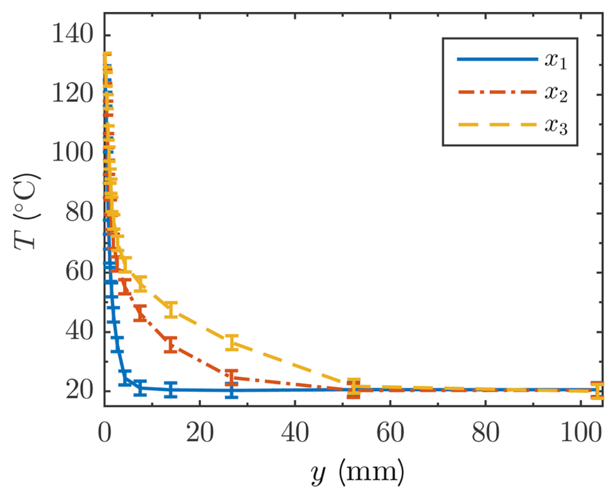

Fig. 13 Measured temperature profiles for all three x locations for the buoyancy-opposed case

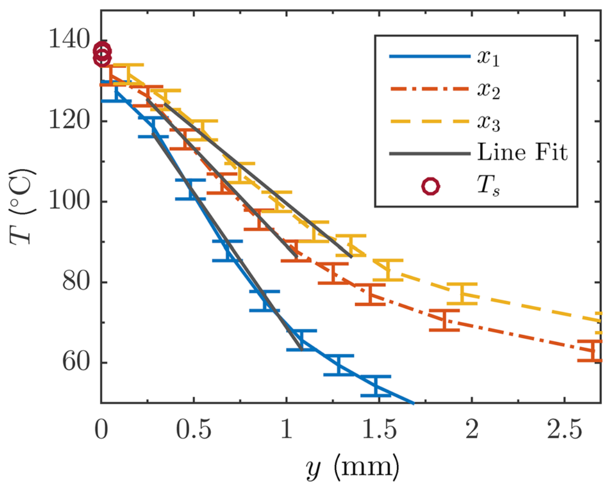

Fig. 14 Measured temperature profiles near the heated wall with line fit for all three *x* locations for the buoyancy-opposed case. Note the unique wall temperature values T_s as the wall is nearly isothermal. T_s at x_1 is about 2 °C cooler than the other two.

probes should be avoided in validation experiments as the effect of their presence is often difficult to quantify. As such, the use of these temperature data is recommended for qualitative analysis but may not be appropriate for quantitative assessment as an SRQ.

Wall heat flux, as measured by the HFSs, is shown in Fig. 15. In laminar flows, buoyancy-aided mixed convection produces higher heat flux values than for buoyancy-opposed [7]. The current experiments show the opposite, suggesting turbulence levels are a major contributor to the flux. These observations are consistent with turbulent mixed convection. As there are no known heat transfer correlations for mixed convection in developing channel flow, the correlation for fully developed flow in vertical tubes was applied as Eq. (6) in the work of Jackson et al. [9]. These are consistent with the observed heat flux as the buoyancy-opposed case generated higher heat flux. The correlation values have been adjusted to consider an unheated starting length with distances from the virtual origin analysis described earlier. The local Nusselt number was adjusted by

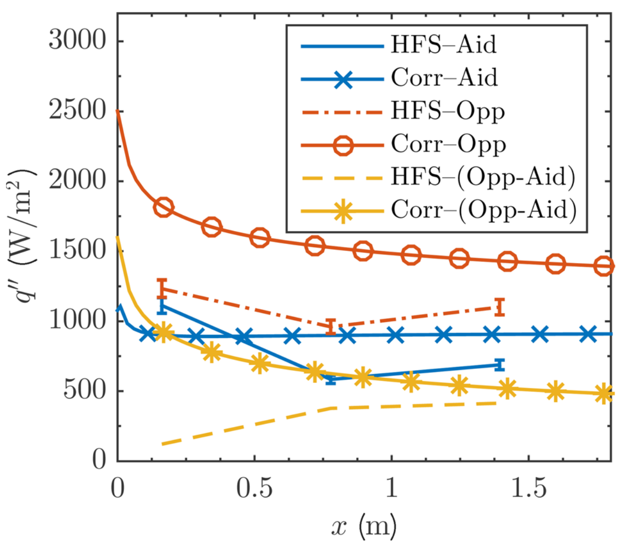

Fig. 15 Measured wall heat flux plotted along streamwise direction *x* with correlations for mixed convection for the bouyancy-aided (Aid), buoyancy-opposed (Opp), and their difference (Opp-Aid). HFS results are labeled as HFS and correlation results as Corr.

$$\mathrm{Nu}_x = \frac{\mathrm{Nu}_x \mid_{\xi=0}}{\left[1-(\xi/x)^{9/10}\right]^{1/9}} \tag{11}$$

where the local Nusselt number Nu_x and $\mathrm{Nu}_x \mid_{\xi=0}$ was measured from the leading edge of the unheated starting length [8].

The measured trends in the streamwise direction x are inconsistent with expected results. The HFS at x_2 gives a smaller reading than that at x_3 for both cases. It is possible that this trend is caused by an installation error of the potted sensors in the heated wall. Even though the cause is unknown, the likelihood of this error existing is supported by the monotonic decrease in the temperature gradient near the wall with streamwise distance x as observed in Fig. 14. This decrease suggests a decrease in the wall heat flux with x, consistent with theory.

Previous methods to quantify wall shear have fit experimental turbulent velocity data with the empirical models such as Spalding or Musker profiles with high accuracy [21]. This method works well for fully turbulent boundary layer data where the models are an accurate representation of velocity, but not for the data in this study due to significant buoyancy effects. Therefore, wall shear stress was estimated directly from PIV data as $\tau_s = \mu(\partial u/\partial y)|_{y=0}$ where τ_s is the wall shear stress and μ is the dynamic viscosity. High-resolution PIV data were used to fit a line to velocity data where $y^+ = yu_\tau/\nu \le 3$ to find $\partial u/\partial y|_{y=0}$, where $u_\tau = \sqrt{\tau_s/\rho}$ and ρ is the fluid density [7]. Initially, ten points were included in the fit and a stable iterative method was used to calculate τ_s and the number of data points that fit within $y^+ \le 3$. The wall was located by the particle images with a mask carefully defined. The linear fit was performed using linear regression with more weight given to velocity data with lower uncertainty [22]. The high-resolution PIV data and associated linear fit are shown in Fig. 16. The dynamic viscosity was evaluated using Sutherland's Law at the wall temperature. The fit uncertainty was combined with the viscosity uncertainty using the Taylor series method for the total shear uncertainty [18].

Data acquisition was repeated several times for each case to determine the level of repeatability. There are generally two repetitions of the same case with the exception of the buoyancy-aided case at x_1, which has three. Data were acquired between one and ten months apart and, in the buoyancy-opposed case, with a different camera. The acquisitions were also performed by two different users. The test section was disassembled, repaired, and reassembled between the second (R2) and third (R3) series for the buoyancy-aided case. The PIV equipment was removed, replaced, and recalibrated between series. The tabulated data included in

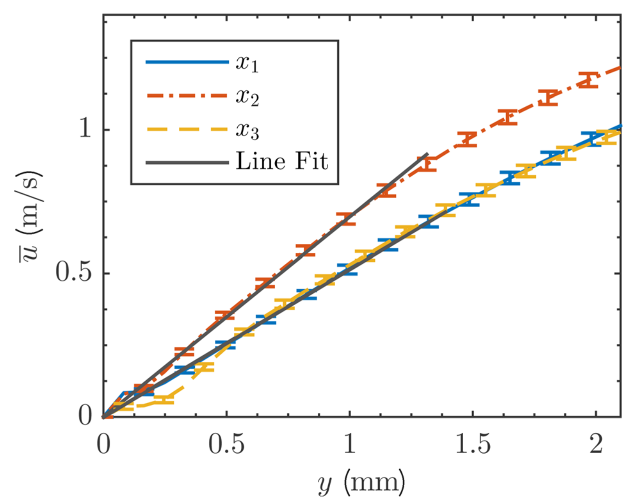

Fig. 16 Streamwise mean velocity $\overline{u}$ near the heated wall with linear fit for shear stress measurement of the buoyancy-opposed case

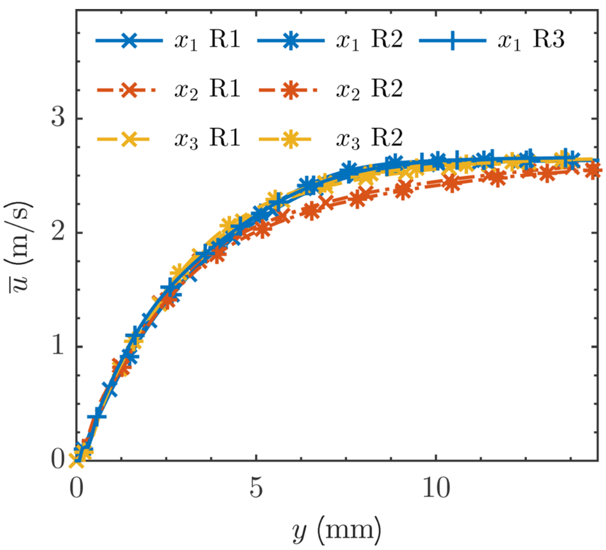

Fig. 17 Mean streamwise velocity $\overline{u}$ with several repeats at three locations in x for the aided case

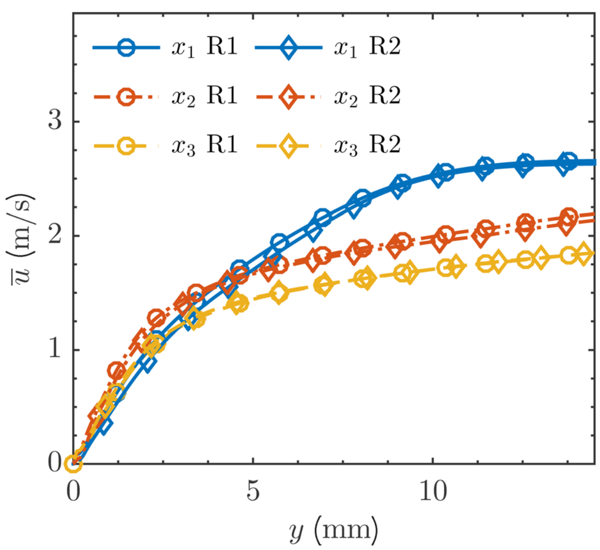

Fig. 18 Mean streamwise velocity $\overline{u}$ with several repeats at three locations in x for the opposed case

this work are from the series R1 in both cases. The results for the mean streamwise velocity are shown in Figs. 17 and 18 for the buoyancy-aided and opposed cases, respectively. They show only small differences that are more apparent in the buoyancy-opposed case.

Repeatability plots for mean streamwise Reynolds stress $\overline{u'u'}$ are shown in Figs. 19 and 20 for the two cases. The Reynolds stresses are less repeatable than the mean velocity, but only by a moderate amount. The results at x_1 have the largest difference, which may be due to differences in the inflow that become less important with streamwise development.

As discussed above, there is a large difference in turbulence levels between the buoyancy-aided and opposed cases. Another method for representing the differences is the scatter plot of $\overline{u'v'}$. There is little scatter in the buoyancy-aided case (Fig. 21) compared to the buoyancy-opposed case (Fig. 22), suggesting that the laminarization is occurring in the buoyancy-aided case. These results are consistent with the findings of other works in turbulent

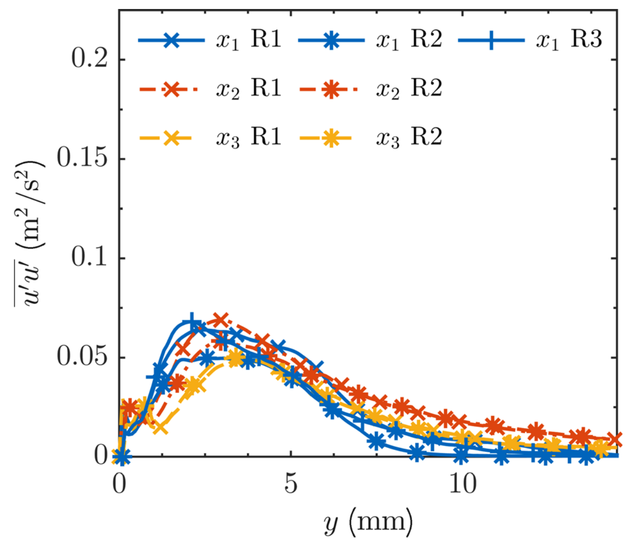

Fig. 19 Measured mean streamwise Reynolds stress $\overline{u'u'}$ with several repeats at three locations in x for the aided case

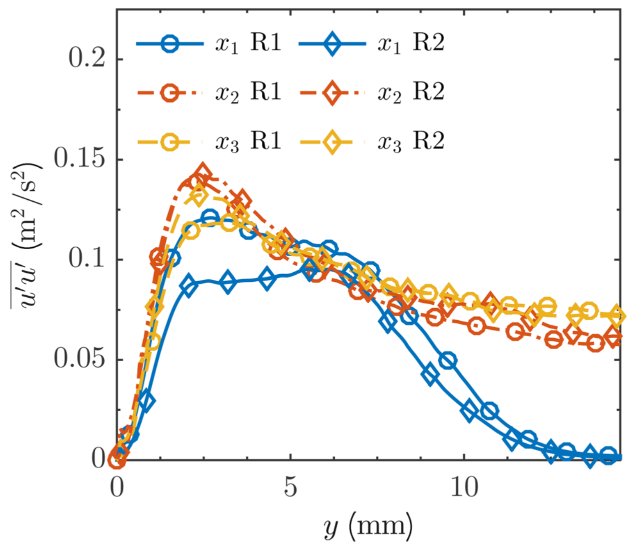

Fig. 20 Measured mean streamwise Reynolds stress $\overline{u'u'}$ with several repeats at three locations in x for the opposed case

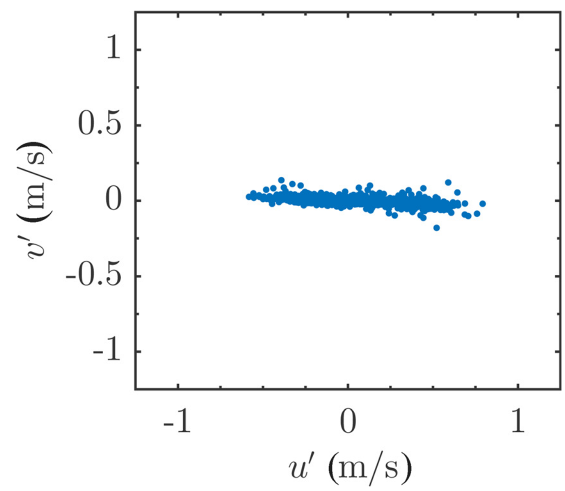

Fig. 21 Scatter of instantaneous u' and v' at the y-location of largest $\overline{u'u'}$ for the aided case at x_2 showing tight grouping

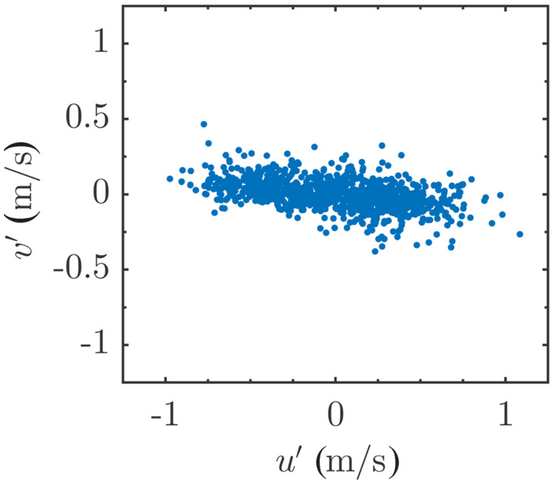

Fig. 22 Scatter of instantaneous u' and v' at the y-location of largest $\overline{u'u'}$ for the opposed case at x_2 showing larger scatter

Table 7 Links to velocity SRQ files for both cases

Aided	Opposed
SRQ-Aid-Vel_x1	SRQ-Opp-Vel_x1
SRQ-Aid-Vel_x2	SRQ-Opp-Vel_x2
SRQ-Aid-Vel_x3	SRQ-Opp-Vel_x3

mixed convection. The results show the typical predominance of events in quadrants 2 and 4, which are related to turbulent ejections and sweeps, respectively.

7.2 SRQ Data. These data are generally found in one file for each x location with unique files for each orientation. For all SRQ files, the same global coordinate system is used and units are included in column headers. Links to the velocity results are found in Table 7. Velocities and Reynolds stresses in both measured directions are given as well as Reynolds shear stress. Uncertainties are provided for all provided quantities.

Temperature profile data are available for the buoyancy-opposed case at all three x locations in files SRQ-Opp-T_x1, SRQ-Opp-T_x2, and SRQ-Opp-T_x3. Tabulated results for the scalar wall heat flux are compiled into the files SRQ-Aid-HeatFlux and SRQ-Opp-HeatFlux. Shear results are similarly compiled into files SRQ-Aid-Shear and SRQ-Opp-Shear.

8 Conclusions

This work has presented a highly detailed study on turbulent mixed convection along a vertical, flat plate using high fidelity instrumentation. The data and description are believed to be sufficient for a CFD validation study of these physics to determine validation error (Eq. (1)) and validation uncertainty (Eq. (2)). The effects of buoyancy were investigated in two orientations, buoyancy-aided and buoyancy-opposed. Buoyancy was found to have a laminarizing effect on the boundary layer flow in the buoyancy-aided case that suppressed heat transfer. The buoyancy-opposed case had increased turbulence levels and higher heat flux. All requisite BCs were measured and provided with their uncertainties. A variety of SRQs were reported for comparison with simulation outputs. Tabulated data are provided by digital links for direct use. This method of data description and dissemination can greatly enhance the ability of modelers to assess simulation accuracy. Furthermore, the inclusion of this information in published works increases their availability.

Acknowledgment

This research was performed using funding received from the DOE Office of Nuclear Energy's Nuclear Energy University Programs.

Nomenclature

- $b_{\bar{x}}$ = standard bias uncertainty of general mean quantity $\bar{x}$
- $B_{\bar{x}}$ = expanded bias uncertainty of general mean quantity $\bar{x}$
- D = experimental data
- D_{TC} = diameter of TC probe wire
- dt = time delay of particle image velocimetry image pairs
- E = model validation error
- g = acceleration due to gravity
- Gr_x = local Grashof number
- N = number of samples
- Nu_x = local Nusselt number
- q''_s = wall heat flux
- Re_x = local Reynolds number
- Ri_x = local Richardson number
- S = simulation result
- s_x = standard deviation of quantity x
- $s\bar{x}$ = standard random uncertainty of mean quantity $\bar{x}$
- $S\bar{x}$ = expanded random uncertainty of mean quantity $\bar{x}$
- T = temperature
- T_s = temperature of wall
- T_∞ = temperature of freestream
- t_{95} = confidence level coefficient at 95%
- $\bar{u}$ = time-mean streamwise (x) velocity
- $\overline{u'u'}$ = time-mean variance of u
- $\overline{u'v'}$ = time-mean covariance of u and v
- $\bar{u}_{\text{bulk}}$ = time-mean streamwise (x) bulk velocity
- $\bar{u}_\infty$ = time-mean streamwise freestream velocity
- U_D = validation data uncertainty
- U_{input} = model input uncertainty
- U_{num} = numeric uncertainty
- U_{val} = validation uncertainty
- $U\bar{x}$ = total expanded uncertainty of mean quantity $\bar{x}$
- u_τ = friction velocity
- $\bar{v}$ = time-mean heated wall-normal (y) velocity
- $\overline{v'v'}$ = time-mean variance of v
- $\bar{w}$ = time-mean transverse (z) velocity
- $\overline{w'w'}$ = time-mean variance of w
- x = streamwise direction
- $\bar{x}$ = general time-mean variable
- y = heated wall-normal direction
- y^+ = nondimensional heated wall-normal direction
- z = transverse direction
- β = volumetric thermal coefficient of expansion
- μ = dynamic viscosity
- ν = kinematic viscosity
- ξ = virtual origin
- ρ = density of air
- τ_s = wall shear stress

References

[1] Oberkampf, W. L., and Smith, B. L., 2014, "Assessment Criteria for Computational Fluid Dynamics Validation Benchmark Experiments," AIAA Paper No. 2014-0205.
[2] Harris, J. R., Lance, B. W., and Smith, B. L., 2015, "Experimental Validation Data for CFD of Forced Convection on a Vertical Flat Plate," ASME J. Fluids Eng., **138**(1), p. 011401.
[3] Oberkampf, W. L., and Roy, C. J., 2010, *Verification and Validation in Scientific Computing*, Cambridge University Press, New York.
[4] ASME, 2009, *ASME V&V 20-2009: Standard for Verification and Validation in Computational Fluid Dynamics and Heat Transfer*, American Society of Mechanical Engineers, New York.
[5] Roache, P. J., 2009, *Fundamentals of Verification and Validation*, Hermosa Publication, Socorro, NM.
[6] AIAA, 1998, "Guide for the Verification and Validation of Computational Fluid Dynamics Simulations," AIAA Paper No. G-077-1998.

[7] Kays, W. M., Crawford, M. E., and Weigand, B., 2012, *Convective Heat and Mass Transfer*, McGraw-Hill, Boston, MA.

[8] Incropera, F. P., Dewitt, D. P., Bergman, T. L., and Lavine, A. S., 2007, *Fundamentals of Heat and Mass Transfer*, 6th ed., Wiley, Hoboken, NJ.

[9] Jackson, J. D., Cotton, M. A., and Axcell, B. P., 1989, "Studies of Mixed Convection in Vertical Tubes," Int. J. Heat Fluid Flow, **10**(1), pp. 2–15.

[10] Chen, T. S., Armaly, B. F., and Ramachandran, N., 1986, "Correlations for Laminar Mixed Convection Flows on Vertical, Inclined, and Horizontal Flat Plates," ASME J. Heat Transfer, **108**(4), p. 835.

[11] Ramachandran, N., Armaly, B. F., and Chen, T. S., 1985, "Measurements and Predictions of Laminar Mixed Convection Flow Adjacent to a Vertical Surface," ASME J. Heat Transfer, **107**(3), p. 636.

[12] Kim, W. S., Jackson, J. D., He, S., and Li, J., 2004, "Performance of a Variety of Low Reynolds Number Turbulence Models Applied to Mixed Convection Heat Transfer to Air Flowing Upwards in a Vertical Tube," Proc. Inst. Mech. Eng., Part C, **218**(11), pp. 1361–1372.

[13] Wang, J., Li, J., and Jackson, J., 2004, "A Study of the Influence of Buoyancy on Turbulent Flow in a Vertical Plane Passage," Int. J. Heat Fluid Flow, **25**(3), pp. 420–430.

[14] Kähler, C. J., Sammler, B., and Kompenhans, J., 2002, "Generation and Control of Tracer Particles for Optical Flow Investigations in Air," Experiments in Fluids, **33**(6), pp. 736–742.

[15] Touloukian, Y. S., and Ho, C. Y., 1977, *Thermophysical Properties of Selected Aerospace Materials Part II: Thermophysical Properties of Seven Materials*, Purdue University, West Lafayette, IN.

[16] Warner, S. O., and Smith, B. L., 2014, "Autocorrelation-Based Estimate of Particle Image Density for Diffraction Limited Particle Images," Meas. Sci. Technol., **25**(6), p. 065201.

[17] Blackwell, B. F., Kays, W. M., and Moffat, R. J., 1972, "The Turbulent Boundary Layer on a Porous Plate: An Experimental Study on the Heat Transfer Behavior With Adverse Pressure Gradients," Stanford University, Stanford, CA, Technical Report No. HMT-16.

[18] Coleman, H. W., and Steele, W. G., 2009, *Experimentation, Validation, and Uncertainty Analysis for Engineers*, Wiley, Hoboken, NJ.

[19] Timmins, B. H., Wilson, B. W., Smith, B. L., and Vlachos, P. P., 2012, "A Method for Automatic Estimation of Instantaneous Local Uncertainty in Particle Image Velocimetry Measurements," Exp. Fluids, **53**(4), pp. 1133–1147.

[20] Wilson, B. M., and Smith, B. L., 2013, "Taylor-Series and Monte-Carlo-Method Uncertainty Estimation of the Width of a Probability Distribution Based on Varying Bias and Random Error," Meas. Sci. Technol., **24**(3), p. 035301.

[21] Kendall, A., and Koochesfahani, M., 2007, "A Method for Estimating Wall Friction in Turbulent Wall-Bounded Flows," Exp. Fluids, **44**(5), pp. 773–780.

[22] Bevington, P. R., and Robinson, D. K., 2003, *Data Reduction and Error Analysis*, McGraw–Hill, New York.